SLAC-PUB-16138

Ultrafast electron kinetics in short pulse laser-driven dense hydrogen

U Zastrau[1,6], P Sperling[2,3], C Fortmann-Grote[4], A Becker[3], T Bornath[3], R Bredow[3], T Döppner[5], T Fennel[3], L B Fletcher[2], E Förster[6,7], S Göde[2], G Gregori[8], M Harmand[9,10], V Hilbert[6], T Laarmann[10,11], H J Lee[2], T Ma[5], K H Meiwes-Broer[3], J P Mithen[8], C D Murphy[12], M Nakatsutsumi[1], P Neumayer[13], A Przystawik[10], S Skruszewicz[3], J Tiggesbäumker[3], S Toleikis[10], T G White[14], S H Glenzer[2], R Redmer[3] and T Tschentscher[1]

[1] European XFEL, Albert-Einstein-Ring 19, D-22761 Hamburg, Germany
[2] SLAC National Accelerator Laboratory, 2575 Sand Hill Road, Menlo Park, CA 94025, USA
[3] Institut für Physik, Universität Rostock, D-18051 Rostock, Germany
[4] QuantumWise A/S, Fruebjergvej 3, DK-2100 Copenhagen, Denmark
[5] Lawrence Livermore National Laboratory, 7000 East Avenue, Livermore, CA 94550, USA
[6] Institut für Optik und Quantenelektronik, Friedrich-Schiller-Universität, Max-Wien-Platz 1, D-07743 Jena, Germany
[7] Helmholtz-Institut Jena, Fröbelstieg 3, D-07743 Jena, Germany
[8] Department of Physics, Clarendon Laboratory, University of Oxford, Parks Road, Oxford, OX1 3PU, UK
[9] Institut de minéralogie, de physique des matériaux et de cosmochimie (IMPMC, CNRS, UPMC, MNHN, IRD), 4 Place Jussieu, F-75005 Paris, France
[10] Deutsches Elektronen-Synchrotron DESY, Notkestrasse 85, D-22607 Hamburg, Germany
[11] The Hamburg Centre for Ultrafast Imaging CUI, D-22761 Hamburg, Germany
[12] School of Physics and Astronomy, University of Edinburgh, Edinburgh EH8 9YL, UK
[13] Extreme Matter Institute, GSI Helmholtzzentrum für Schwerionenforschung, D-64291 Darmstadt, Germany
[14] Institute of Shock Physics, Imperial College London, London, SW7 2AZ, UK

E-mail: ulf.zastrau@xfel.eu

Received 3 May 2015, revised 14 June 2015
Accepted for publication 15 June 2015
Published 25 September 2015

Abstract

Dense cryogenic hydrogen is heated by intense femtosecond infrared laser pulses at intensities of $10^{15} - 10^{16}$ W cm^{-2}. Three-dimensional particle-in-cell (PIC) simulations predict that this heating is limited to the skin depth, causing an inhomogeneously heated outer shell with a cold core and two prominent temperatures of about 25 and 40 eV for simulated delay times up to +70 fs after the laser pulse maximum. Experimentally, the time-integrated emitted bremsstrahlung in the spectral range of 8–18 nm was corrected for the wavelength-dependent instrument efficiency. The resulting spectrum cannot be fit with a single temperature bremsstrahlung model, and the best fit is obtained using two temperatures of about 13 and 30 eV. The lower temperatures in the experiment can be explained by missing energy-loss channels in the simulations, as well as the inclusion of hot, non-Maxwellian electrons in the temperature calculation. We resolved the time-scale for laser-heating of hydrogen, and PIC results for laser–matter interaction were successfully tested against the experiment data.

Keywords: electron collisions, emission, absorption, and scattering of electromagnetic radiation, plasma production and heating by laser beams

(Some figures may appear in colour only in the online journal)

This material is based upon work supported by the U.S. Department of Energy, Office of Science, Office of Basic Energy Sciences, under Contract No. DE-AC02-76SF00515.

1. Introduction

Dense plasma states are relevant for a wide variety of astrophysical objects such as stars and planets throughout the universe [1, 2]. Furthermore, they are generated in the laboratory by isochoric heating using intense x-ray or particle beams or various shock compression techniques. Progress in plasma theory has lead to the development of *ab initio* methods which, in principle, enable accurate predictions for the behavior of matter under such extreme conditions [3]. However, our knowledge on dense plasma states is still very limited and joint efforts of astrophysics and planetary physics, laser and plasma physics and high pressure physics have to be performed in order to get more insight into the behavior of matter in this region. For instance, the equation-of-state (EOS), the transport properties like electrical and thermal conductivity, the ionization and recombination dynamics, and the opacity of dense plasmas are known only for few states of pure substances (e.g. hydrogen, helium, carbon, aluminum, iron, water) but urgently needed also for mixtures such as H-He (stars, Jupiter-like planets), water-ammonia-methane (Neptune-like planets), or various minerals of the SiO_2-MgO-FeO complex (Earth, super-Earths), see [4, 5].

Astrophysically relevant systems have typical energy densities in excess of $10^5\,\mathrm{J\,cm^{-3}}$, equivalent to the binding energies of condensed matter. In particular, dense hydrogen is currently in the focus of a world-wide effort to determine its EOS and other physical properties. Amongst other applications EOS data is needed for realistic models for the interior of giant planets such as Jupiter. Standard models assume a molecular non-conducting outer fluid layer, a conducting fluid layer below, and the possibility of a central solid core [6]. The chemical composition throughout the layers, the location of the layer boundaries, and the size of the core are adjusted to reproduce the observational constraints. However, a complete verification of the planetary structure model is still missing and requires experimental data for the EOS, conductivity, and opacity of H and He [7–9]. Recently, we evaluated Saha-like and QEOS-like [10] EOS to model experimental data of equilibration dynamics [11].

In our experiments, intense sub-picosecond x-ray ultraviolet (XUV) laser pulses ($1\,\mathrm{ps} = 10^{-12}\,\mathrm{s}$) allow for isochoric heating, which deposits energy into the sample on a timescale much shorter than hydrodynamic expansion (cf figure 1). Hence, by probing at a certain time delay during the plasma evolution, the transient plasma properties can be extracted.

These dense plasmas are strongly correlated systems. Pronounced deviations from the ideal gas behavior result and partial ionization and electron degeneracy have usually to be considered. Furthermore, nonmetal-to-metal transitions may appear, both pressure and temperature driven, and transitions between various high pressure phases may occur. Microscopic properties of dense matter related to reflectivity, electrical and thermal conductivity are tied to dynamic energy exchange between electrons and ions. On a macroscopic scale, these properties affect, e.g., the depth of mixing layers in Jovian planets [15], as well as the formation of a central hot spot and the assembly of thermonuclear fuel layers in inertial confinement fusion implosions [16–18].

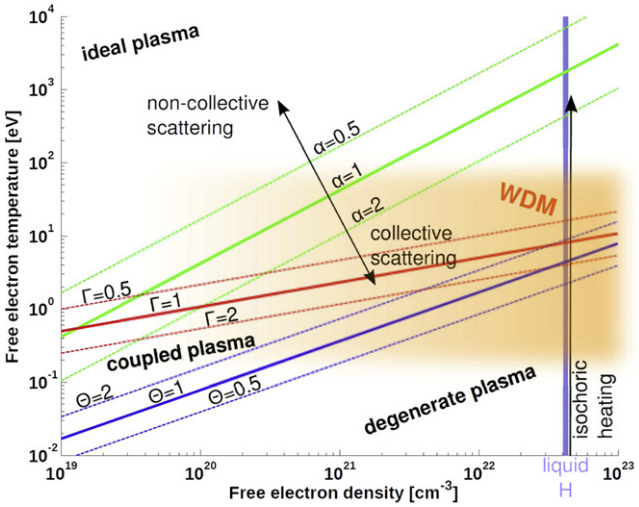

Figure 1. Electron temperature T_e as function of density n_e. The coupling parameter Γ is defined as the ratio of the Coulomb energy between two charged particles and the thermal energy. It divides the phase space into ideal ($\Gamma \ll 1$), weakly coupled ($\Gamma \leqslant 1$), and strongly coupled ($\Gamma \gg 1$) plasmas. The degeneracy parameter Θ, which is the ratio of thermal energy and the Fermi energy, divides the phase space into areas where quantum effects are of importance ($\Theta < 1$, degenerated plasmas) and areas where the role of quantum effects decreases ($\Theta > 1$). The density of liquid hydrogen (blue vertical line) and the warm dense matter (WDM, orange) regime are indicated. The scattering parameter α is the ratio of probed scale length to the Debye screening length for 13.5 nm radiation [12] as used in our previous study [11, 13]. *Figure reproduced from* [14] (c) Elsevier BV

The accessible parameter space depicted in figure 1 can be probed by several approaches. In classical plasma spectroscopy, the ratio of characteristic emission lines allows to infer the plasma temperature and ion abundance. However, all methods employing visible radiation suffer from the overdense plasma, limiting the diagnostic to the surface. In the last decade, inelastic x-ray scattering has proven to be a reliable tool for volumetric studies of dense plasmas [19]. For dense hydrogen, we derived the free-electron density and temperature from the collective plasmon scattering spectrum via the so-called detailed-balance relation [20]. This method is applicable in the region where the scattering parameter $\alpha \sim 1$ (green line in figure 1).

Recently, we have shown that elastic scattering gives access to ultrafast dissociation dynamics and conductivity. Cryogenic hydrogen at $0.08\,\mathrm{g\,cm^{-3}}$ solid density was isochorically heated. Here, electrons were photo-ionized by a multi-terawatt soft x-ray burst of duration $\leqslant$300 fs [11, 13]. A second pulse probed the microscopic sample structure via x-ray scattering at a variable time delay. As shown in figure 2, the initial molecular structure dissociates within (0.9 ± 0.2) ps due to relaxation processes between electrons and atoms/ions.

Even though XUV rays heat dense hydrogen homogeneously, it yielded an ionization degree of only $<10\%$ and ion temperatures $k_B T_i < 0.5$ eV ($T_i < 6400$ K) [11].

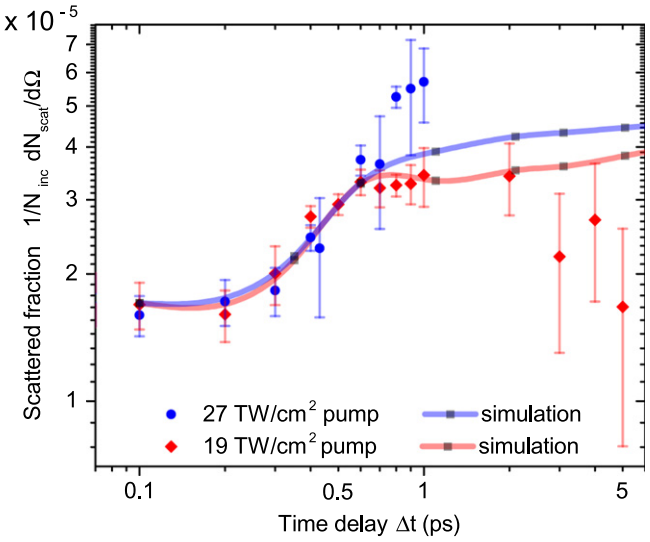

Figure 2. Results of XUV-heated dense hydrogen from [11]. Shown is the temporal evolution of the measured (symbols) and simulated (lines) scattering of 13.5 nm photons. For the blue points, ranging from $\Delta t = 0$ to 1 ps only, the more intense 27 TW cm^{-2} pulse pumps the target, while it is probed by the 19 TW cm^{-2} pulse. The red diamonds, ranging from 0 ps to 5 ps, resemble the inverse case where the pump was less intense (19 TW cm^{-2}) than the probe (27 TW cm^{-2}). In both cases, the signal increases within 1 ps, and for the more intense pump the amplitude is larger. The red and blue lines represent the simulated scattered fraction using a Saha-like ionization model.

Generation of hotter and potentially denser plasma can be achieved by intense optical laser irradiation. When the rising edge of an intense laser pule generates the first free electrons via tunnel ionization, the critical density is reached, the refractive index becomes imaginary and light penetration is limited to the skin depth of a few 10 nm. There, it causes strong but inhomogeneous heating of the target.

However, an accurate description of the laser–matter interaction as well as a reliable prediction of the laser-generated plasma parameters such as temperature and density, especially for high-intensity laser pulses on short time-scales below 10 ps, is still missing. In particular free electrons are produced via tunnel ionization in the skin depth and accelerated in the laser field. Via impact ionization, they heat the interior of the target [21, 22]. This is an important effect for the fundamental understanding of the laser-driven generation of plasmas on ultra-short time scales [20, 23], the excitation of clusters [24, 25], and for applications like inertial confinement fusion.

In our earlier studies [11], the temperature was determined indirectly by hydrodynamics simulations, which turned out to be extremely sensitive to the proper choice of the EOS. Further, modeling the nonlinear absorption mechanisms of optical laser poses a challenge to hydrodynamic modeling. Hence, an experimental temperature determination is critically needed. In this paper, we determined the electron temperature distribution within an optical laser-irradiated cryogenic hydrogen target on a sub-ps time-scale using XUV bremsstrahlung spectroscopy.

2. Experiments

In classical plasma spectroscopy, ratios of characteristic emission lines are employed for the purpose of temperature determination. The hydrogen spectra series lies dominantly in the visible and infrared spectral range, where probed states have long lifetimes. Optical emission also interferes with scattered laser light and possible higher-harmonic generation during the excitation process. Only the Lyman series emits in the ultraviolet spectral range (91–121 nm) and could be of interest for future experiments.

In this work, we determine the temperature of the free electrons in the plasma by measuring the continuum radiation (bremsstrahlung) in the XUV spectral range (in our case, wavelengths of 10–20 nm, corresponding to photon energies of 62–124 eV). Since the emissivity J_{ff} of bremsstrahlung scales as $J_{\mathrm{ff}} \propto n_{\mathrm{e}}^2$ (n_{e} is the free electron density), our method is sensitive to the scientifically interesting regions of increased ionization at high density, while the cold dense plasma background, as well as ionized dilute residual hydrogen gas, do not contribute.

2.1. Hydrogen jet target

The cryogenic hydrogen source has been previously described [26]. Here, we summarize the most important parameters.

To provide a near-solid density state of hydrogen the use of a cryogenic liquid or solid target is mandatory. The controlled production of microscopic streams of a material is a challenging task. In particular for plasma spectroscopy, a cryogenic hydrogen source provides a free-standing target in vacuum suitable for experiments at high repetition rate.

Generally, the principle of operation is to press gas through a small orifice into vacuum in a way that a continuous liquid filament is formed. Since a liquid stream is unstable against its surface tension, small fluctuations will grow and the so-called Rayleigh breakup [27] will destroy the jet after a characteristic distance of propagation. The jet or broken-up fragments freeze by evaporational cooling and form solid droplets after several millimeters in flight.

We employ a temperature-controlled helium flow cryostat to cool down the nozzle and the hydrogen supply line to a temperature in the range of 20 K. The hydrogen stagnation pressure in our experiment is typically 2 bar which results in a velocity of about 60 m s^{-1} of the liquid filament. We note that within a picosecond—the upper limit of the time delays under considerations in the present study—the jet moves only by ~60 pm and hence can be assumed to be at rest. The maximum tolerable background pressure in the vacuum chamber limits the nozzle diameter to a maximum of 20 μm. However, in the present experiments, the chosen nozzle diameter of 5 μm results in an estimated filament diameter of 8–10 μm.

A photograph of the hydrogen liquid jet in operations is shown in figure 3. The cryostat is mounted on a three-dimensional manipulator to provide the alignment to the FEL and XUV spectrometer focus volume, respectively. The interaction point has been set ~1–2 mm away from the nozzle exit.

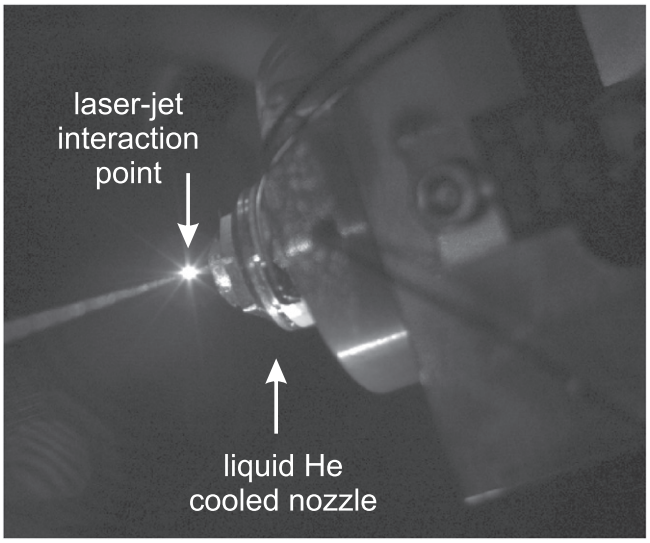

Figure 3. The liquid hydrogen jet operational in high vacuum, as viewed from a long-range microscope outside the vacuum chamber.

2.2. Titanium:Sapphire laser system

The FLASH FEL experimental infrastructure [28, 29] at DESY (Hamburg) provides a so-called *pump-probe* laser system. Details can be found in [30]. Here, we give only the characteristics relevant to this publication. A Ti:sapphire oscillator produces ultrashort pulses that are synchronized to the master clock of FLASH. Two different amplifier systems are available: the first one is low-energy (μJ-level) chirped-pulse optical parametric amplifier (OPCPA) which can operate at the full MHz burst mode of FLASH.

However, in order to generate plasmas, synchronized laser pulses in the mJ energy range are provided by a second amplifier system. The Ti:sapphire oscillator pulses are amplified to $\leqslant$20 mJ by a chirped pulse amplifier system, which consists of a regenerative and a two-pass amplifier. Due to the architecture of this laser system the repetition rate is limited to 10 Hz.

Since 20 mJ at typical 50 fs pulse duration equals 0.4 TW of peak power in a 10 mm diameter beam such pulse tends to break up into filaments while propagating in air. Therefore for pulse energies above 1 mJ the pulse duration has to be elongated to several ps to transport the beam. In our experiment, the laser pulse was re-compressed with a transmission-grating setup located close to the experiment.

After the compressor, the 800 nm laser pulses were focused by a lens to a $\sim$30 μm FWHM Gaussian beam spot into the center of the vacuum chamber, where a residual gas pressure of the order of 10^{-6} mbar was established. The laser energy was measured by a calorimeter to be $\sim$12 mJ. After re-compression at the experiment, a pulse duration of (80 ± 20)fs was measured by an auto-correlator setup. This yields a typical intensity of $I = 2 \cdot 10^{16}$ W cm^{-2} on target.

As sketched in figure 4, the liquid hydrogen jet (see section 2.1) is injected horizontally into the vacuum chamber at an angle of about 110°—almost perpendicular—to the optical laser. The laser light is linearly polarized in the same plane (along the y-axis in figure 4) as the hydrogen jet.

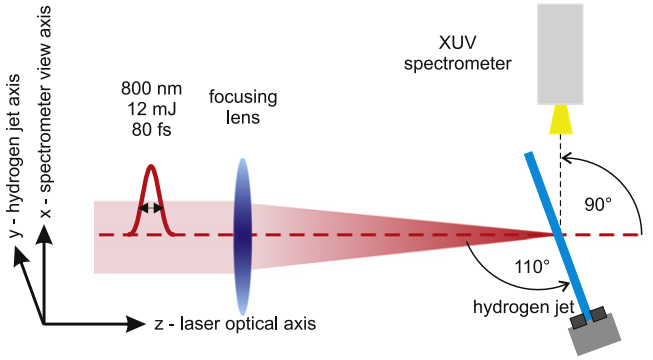

Figure 4. Schematic of the experimental setup. The optical fs-laser is focused onto a cryogenic hydrogen jet at an angle of $\sim$110°. The laser is horizontally polarized along the jet direction. Soft x-ray emission is recorded by an XUV spectrometer at 90°. For further details refer to the text.

2.3. XUV spectroscopy

In the experiment, the compact soft x-ray spectrograph HiTRaX [31] was employed. It covers a wavelength range of 5–35 nm and comprises a toroidal mirror and a variable line space reflection grating. The spectrum is imaged onto a Princeton Instruments back-illuminated CCD camera with a pixel size of 13.5 × 13.5 μm^2 on a 2048 × 512-pixel chip and air-cooled Peltier elements. In the HiTRaX design, particular emphasis has been placed on achieving a large acceptance angle and a high efficiency of the components.

The instrument achieves a resolution $\lambda / \Delta\lambda = 330$, which was measured from the width of a plasma line at 21 nm [31]. The instrument is housed inside a DN100 CF ultra high vacuum-manipulator which allows precise positioning relative to the interaction volume. The spectrometer is equipped with a motorized filter wheel with free-standing thin-foil filters (Al, Zr) of 200 nm thickness and a shutter.

Further details on the XUV spectrometer can be found in [43]. Here, we report on the determination of nonlinear dispersion function. An optical laser pulse is focused onto a target made of technical aluminum. Technical aluminum (or *Duraluminium*) is an alloy of aluminum (which alone is rather soft and greasy) with traces of magnesium, manganese and/or silicon. Typical alloys are AlMg4.5Mn and AlMgSi0.5. Upon laser interaction, a plasma with a rich emission line spectrum is generated. In the XUV wavelength range of 10–19 nm, the spectrometer is calibrated using tabulated emission lines (figure 5). The corresponding transitions, term configurations and wavelengths (marked as black symbols in the figure) can be found in [43]. This cross-calibration is performed *in situ* during the experimental campaign on cryogenic hydrogen. This method allows for precise absolute spectral dispersion calibration.

3. Modeling

3.1. Particle-in-cell (PIC) simulations

The critical density n_c is defined at the equality of the plasma frequency $\omega_P = \sqrt{n_e e^2 / \epsilon_0 m_e}$ and the laser frequency ω (e is

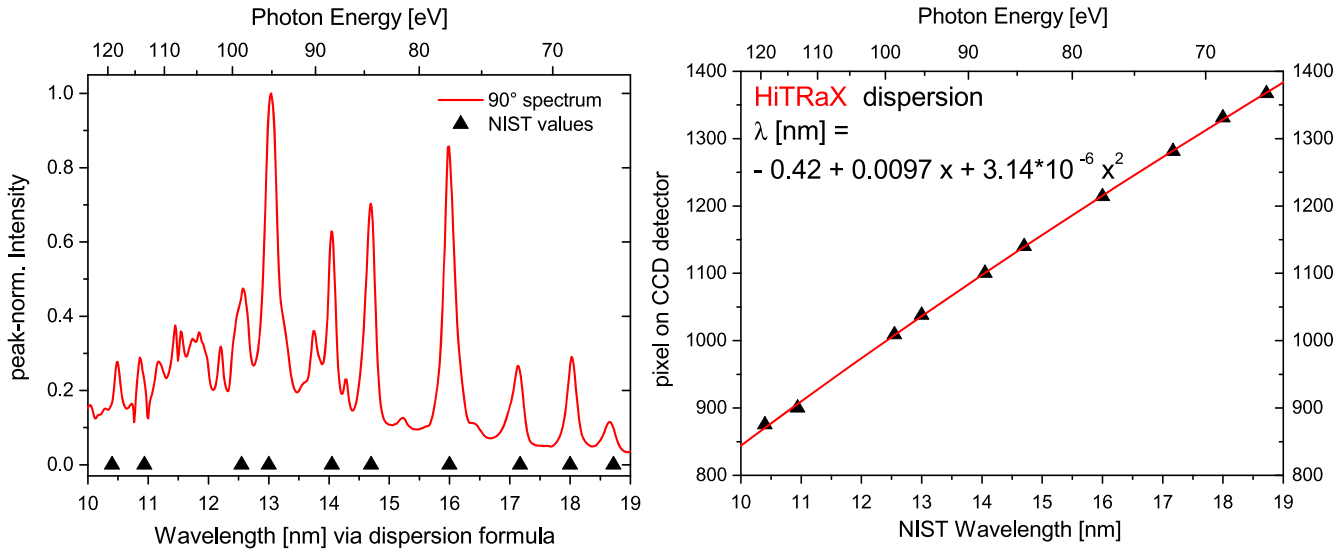

Figure 5. *Top*: the Spectrum from a laser-irradiated Al:Mg alloy is shown. The black rectangles represent the emission lines with known wavelengths. These values are taken from the NIST atomic spectra database (ASD). *Bottom*: the dispersion function of the HiTRaX XUV spectrometer is plotted against the absolute CCD pixel position. The x-axis in nm (bottom) and eV (top) indicate the spectral coverage.

the elementary charge, ϵ_0 is the dielectric constant, and m_e is the electron's mass). At higher electron densities, electromagnetic waves are shielded. For optical lasers $n_c \sim 10^{21} - 10^{22}$ cm^{-3}, and hence volumetric penetration is limited to dilute plasmas. In general, a dense target is heated inhomogeneously. This is driven by various effects induced by the laser field, e.g. tunnel ionization [33], bremsstrahlung, wake-field generation, self-focusing [34], the Brunel effect [35], resonance absorption [36], and $J \times B$ heating [37], and can be simulated by three-dimensional PIC codes solving Maxwell's equations [38].

The interaction of a hydrogen droplet with the optical laser was simulated with the three-dimensional PIC code described in [39]. In the simulations, the peak intensity of the optical laser with wavelength $\lambda = 800$ nm, intensity $I = 10^{15}$ W cm^{-2}, and pulse duration $t_{\mathrm{FWHM}} = 90$ fs irradiates the droplet surface at $\Delta t = 0$ fs. The laser pulse was assumed as plane wave due to the small hydrogen droplet, which—due to computational constrains—had a radius of only $r_{\mathrm{droplet}} = 2\,\mu$m in the simulation, as compared to the laser focal spot size of $r_{\mathrm{laser,\ FWHM}} = 20\,\mu$m. The laser interaction with the hydrogen target with an initial density of 5.1×10^{22} cm^{-3} was simulated on $600 \times 600 \times 600$ cells within a box of $5.6 \times 5.6 \times 5.6\,\mu$m^3. The 125 particles per cell were resolved within time steps of $\Delta t = 2.66$ as.

3.2. Bremsstrahlung modeling

In the year 2008, we were the first to employ the intense XUV pulses of the FLASH facility [28] to isochorically heat aluminum samples [40]. We observed a non-zero continuum radiation in the XUV emission spectrum (XES). The signal intensity increases with stronger excitation [41], which supports the interpretation as XUV bremsstrahlung. We analyzed the XES from bulk aluminum irradiated at FLASH intensities of 10^{14} W cm^{-2} [42]. The electron temperature T_e and density n_e were inferred from fundamental relations.

We compared the experimental data to the theoretical bremsstrahlung emissivity (radiated energy per unit wavelength interval and per unit time into 4π solid angle) [43],

$$J_{\mathrm{ff}}(\lambda) = \left(\frac{e^2}{4\pi\epsilon_0}\right)^3 n_e^2 \cdot \frac{16\pi Z e^{-2\pi\hbar c/\lambda k_B T_e}}{3 m_e c^2 \lambda^2 \sqrt{6\pi k_B T_e m_e}}\, g_T(\lambda). \qquad (1)$$

Here, m_e is the electron mass and $g_T(\lambda)$ is the wavelength dependent Gaunt factor [44], accounting for medium and quantum effects. It is calculated in the Sommerfeld approximation [45]. In our earlier studies [40], statistical analysis of the data yielded 40.5 eV for the plasma free-electron temperature within the aluminum plasma with an RMS error of ±5.5 eV. Hence XUV bremsstrahlung is a sensitive diagnostic, and we proved that we can efficiently heat solid targets.

Furthermore, we note that the emissivity scales as $J_{\mathrm{ff}} \propto n_e^2/\sqrt{T_e}$. In particular, the quadratic scaling with the free-electron density n_e allows for an estimate of this quantity via the intensity of the recorded bremsstrahlung signal when absolutely calibrated spectrometers are used. This fact indicates that our method is weighted towards dense regions of increased ionization, while the cryogenic hydrogen, as well as hot dilute gas, does not significantly contribute.

4. Results

4.1. XUV spectra predicted by PIC simulations

Figure 6 shows results from PIC-code simulations. The optical laser irradiates the droplet from the left and tunnel ionizes the surface within the skin depth. Two-dimensional cuts through the laser polarization plane of the plasma free-

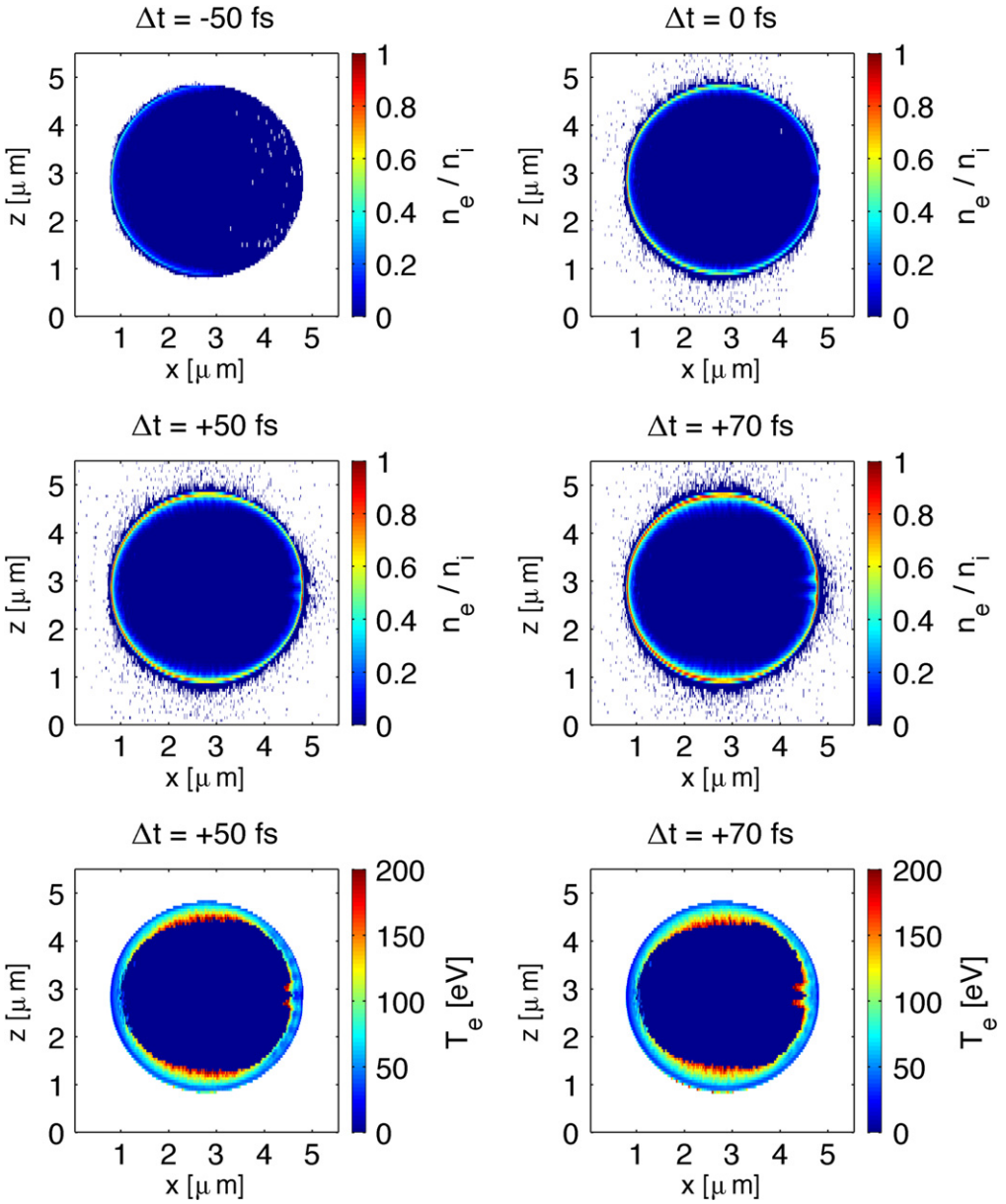

Figure 6. PIC simulations of the free-electron density (top and middle row) and temperature (bottom row) of the cryogenic hydrogen droplet, irradiated with an optical laser pulse, for various delay times Δt. The electron density is normalized to the initial ion density, as function of time. The figures show two-dimensional cuts along the laser polarization plane, where the optical laser impinges from the left. It reaches its maximum intensity at the droplet front at $\Delta t = 0$ fs, while the FWHM intensity is assumed at ±45 fs.

electron density (top rows) at time delays ranging from −50 fs to +70 fs show results during laser irradiation. At the left droplet boundary, the laser pulse reaches its maximum intensity at $\Delta t = 0$ fs, while the FWHM intensity points are assumed at ±45 fs. Initially, only the droplet surface is ionized and heated. Subsequently, electrons are accelerated outwards into vacuum and also into deeper hydrogen layers. The bottom row of figure 6 illustrates the electron temperature. The electron temperature is calculated via $\overline{E}_{\mathrm{kin}} = \frac{3}{2} k_{\mathrm{B}} T_{\mathrm{e}}$ on $600 \times 100 \times 100$ boxes combining neighboring cells. A local thermal equilibrium within the electronic subsystem is assumed for times $\Delta t \geqslant 50$ fs.

The underlying mechanism is surface heating by the optical laser within the skin depth, and subsequent heat transport by electrons into the deeper droplet interior. Due to the surface heating, the variation of electron temperature along the droplet radius is strong—while most of the droplet interior remains cold for delay times <50 fs, the surface is heated to temperatures of several tens of eV, with local hot spots reaching up to 200 eV. Regions with increased free-electron density (cf figure 6) coincide with elevated free-electron temperatures, but not exceeding 100 eV.

Free electrons will undergo inelastic collisions with the electrons and protons, which leads to the emission of bremsstrahlung. The shape of the bremsstrahlung spectrum is sensitive to the electron temperature distribution in the plasma. The red curve in the top graph of figure 7 shows the probability to find electrons in the simulated three-

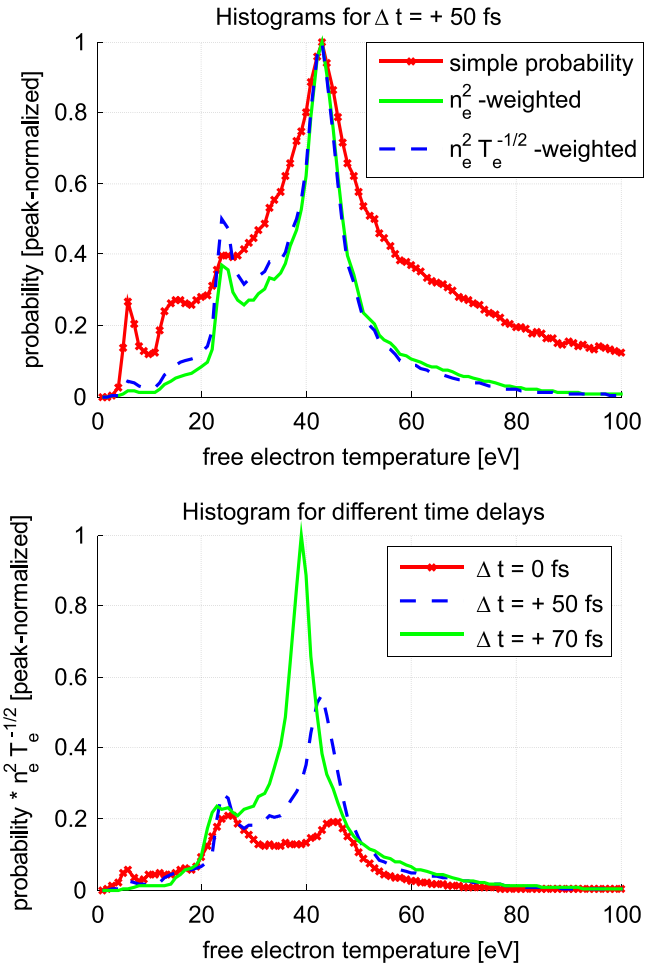

Figure 7. *Top*: simulated probability of electrons in the three-dimensional droplet as function of temperature in a histogram, for a time delay of $\Delta t = +50$ fs. Shown are the simple probability and two probabilities weighted according to equation (1). *Bottom*: histogram of the $n_e^2/\sqrt{T_e}$-weighted temperature distribution for three different time delays.

dimensional droplet from the PIC simulations presented in figure 6 in a histogram with 1 eV-bins, for a time delay of $\Delta t = +50$ fs. A temperature of around ∼43 eV has the highest probability.

According to equation (1) the free-free emissivity J_{ff} of bremsstrahlung scales as $J_{\mathrm{ff}} \propto n_e^2/\sqrt{T_e}$. Hence the electron populations have to be weighted with respect to these—spatially varying—ratios in order to reflect their contribution to the bremsstrahlung emission. When weighted by $n_e^2(\vec{r})$ (green curve), a second peak at 25 eV becomes prominent and the electron contribution with temperatures >80 eV and <20 eV is strongly reduced. Additional weighting by $1/\sqrt{T_e(\vec{r})}$ (blue curve) only slightly alters the probability distribution, enhancing the low-temperature part of the spectrum.

The lower graph of figure 7 shows the $n_e^2/\sqrt{T_e}$-weighted temperature distribution for three different time delays. At the laser pulse maximum ($\Delta t = 0$ fs) we have two prominent temperatures peaks present in the plasma: (i) ∼25 eV and (ii) ∼45 eV. With evolving time, the amplitude of the high-T_e peak rises by a factor of 5, while its temperature drops to 39 eV at $\Delta t = 70$ fs. The lower temperature peak stays about constant in both amplitude and position. We note that at $\Delta t > 70$ fs the pump laser pulse is off and no additional energy is transferred to the system.

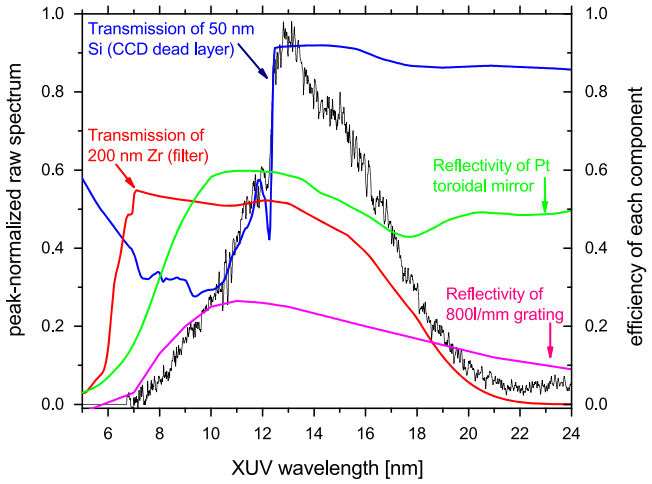

Figure 8. Raw spectrum (black line) of the XUV bremsstrahlung emitted by the hydrogen target, together with the efficiency of the optical components in the HiTRaX XUV spectrometer.

4.2. Measured XUV spectra

The optical laser irradiated the cryogenic hydrogen jet at a repetition rate of 10 Hz. XUV spectra were recorded with an acquisition time of 60 s each, yielding an accumulated spectrum of 600 exposures on the detector. The laser was operated at full intensity ($2 \cdot 10^{16}$ W cm^{-2}), 30%, and 10% intensity by introducing optical density filters. A raw background-corrected profile for the case of full laser intensity is shown in figure 8. As can be seen, to unfold the spectral shape of the emission spectrum, the wavelength-dependent reflectivity, transmission, and efficiency need to be accounted for, which are taken from vendor specifications or are calculated. The 200 nm thin zirconium (Zr) filter—used to suppress optical stray light from the laser—has a transparency window from ∼6 to 22 nm. The Pt-coated toroidal mirror and diffraction grating of the spectrometer only reflect wavelength >6 nm due to the wavelength-dependence of total external reflexion.

While these components yield a smooth shaping of the spectrum, a distinct, sharp feature was identified at 12.3 nm. It can be understood by means of photo absorption of silicon (Si) inside the CCD chip. The amplitude of the Si L absorption edge at 12.3 nm in the measured spectra yields an effective thickness of 50 nm at solid density. When the raw spectrum is corrected for the influence of these components, a smooth continuum is derived as shown in figure 9.

In order to obtain absolute photon numbers, the spectrum is normalized to a single laser exposure, to the solid angle $\Delta\Omega = 0.0245$ sr of the spectrometer, and to spectral bins of constant width of $\Delta\lambda = 1$ nm. The wavelength-dependent quantum efficiency of the CCD is taken into account, as well as the conversion factor of one electron-hole pair per 3.6 eV photon energy.

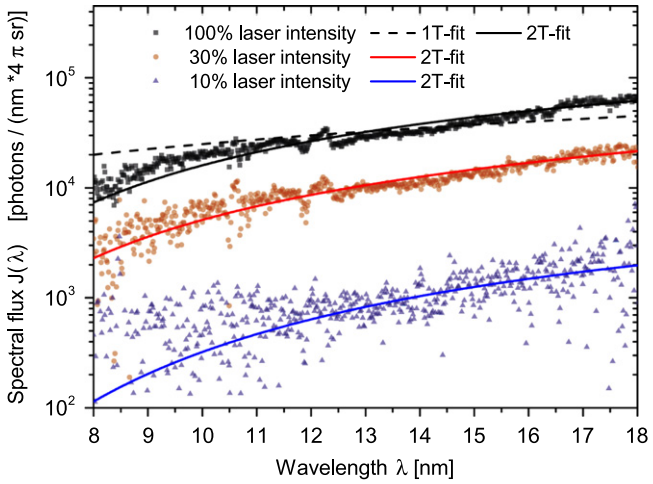

Figure 9. Spectral flux $J(\lambda)$ of the XUV bremsstrahlung emitted from the hydrogen target. The points are measured spectra for three different laser intensities, shown on an absolute logarithmic scale. The lines are bremsstrahlung fits to the data.

The symbols in figure 9 show three experimental spectra for 100%, 30% and 10% laser intensity, where 100% corresponds to $I = 2 \cdot 10^{16}$ W cm^{-2}. These spectra have been sensitivity-corrected as shown in figure 8. The structure at ∼12 nm is an artifact from the correction for the infinitely sharp Si L-absorption edge from tabulated data and the experimental edge measured with finite resolution.

The low-noise part of the spectrum between 8 and 18 nm is used to fit a bremsstrahlung spectrum. The dashed line in figure 9 is the best single-temperature fit to the 100% -intensity spectrum, yielding a temperature of $k_B T = 4.9$ eV. No single temperature can reproduce the slope of the measured data within the observed spectral range. Therefore, we use two independent temperatures T_1 and T_2, plus the weight ratio of the respective spectra, denoted as T_2/T_1, for fitting the data. The results are indicated by the solid lines. The resulting fit spectrum was normalized to the integral of the photons emitted in the spectral range $8 - 18$ nm.

The obtained values for the two temperatures and their respective weight are as follows:

Intensity	$k_B T_1$	$k_B T_2$	weight T_2/T_1
10%	14.5 eV	26.5 eV	0.540
30%	12.4 eV	31.9 eV	0.179
100%	14.1 eV	33.3 eV	0.418

Hence, a two-temperature model is in good agreement with the experimental data: bremsstrahlung emitted by free electrons at a temperature of 12.4–14.5 eV is superimposed by a second spectrum emitted by electrons with a higher temperature of 26.5–33.3 eV.

5. Discussion

In the experiment, we found that in the detectable wavelength range of 8–18 nm flat, continuous XUV spectra are emitted. Residual structure in the spectra results from absorption edges in the detection system. The spectra are best fit with a bremsstrahlung model which accounts for two temperatures of ∼13 and ∼30 eV. When the laser intensity is reduced from 100% to 30% and 10%, the hotter temperature decreases from 33.3 to 31.9 eV and finally to 26.5 eV. The lower temperature does not change systematically with laser intensity.

From the PIC simulations it can be assumed that a dominant temperature of ∼40 eV is established on the plateau of the collision front, where surface-heated electrons collide with the cold bulk matter. Before and after the collision front, the temperature varies, leading to gradients. A second, colder temperature of ∼25 eV represents the average temperature of equilibrated electrons in the dense regions of the target.

We note that the experimental observation of two pronounced temperatures is in agreement with the results from the PIC simulations, but the overall temperatures are 25–50% higher in the case of the simulation. In the calculation of the electron temperature from the PIC results, all electrons have been accounted for, including the hot ones which do not contribute to a physically relevant temperature in the sense of a Maxwell distribution. These yield to an overestimation of the plasma temperature. Also, the PIC simulations do not account for Coulomb collisions, which alter the energy partition towards higher free-electron densities and lower electron temperatures. We note that the general good agreement between experiment and simulation indicates low sensitivity to the smaller target size in the simulations, the different target geometry (jet versus droplet) and differences in laser intensity. Effects like laser pre-pulses on the few-nanosecond time-scale potentially alter the heating mechanism. In our experiment, pre-pulses at 1–2 ns before the main pulse have a measured intensity contrast ratio of a few 10^{-4}, but were neglected in the PIC simulations. The good agreement between experiment and simulation indicates that in our case pre-pulse heating does not seem to play a relevant role for XUV bremsstrahlung spectroscopy as a reliable plasma diagnostics.

6. Conclusion

In this paper, we evaluate heating of dense cryogenic hydrogen by intense fs infrared laser pulses and compare the achievable temperatures to experiments using fs XUV pulses. We further measure the free-electron temperature in a dense hydrogen plasma, which is superior to earlier experiments where the plasma temperature was only simulated using hydrodynamics calculations.

In three-dimensional PIC simulations a 4 μm diameter droplet was irradiated by a 800 nm laser pulse at an intensity of 10^{15} W cm^{-2} and a pulse length $t_{FWHM} = 90$ fs. The electron heating is limited to the skin depth, causing an inhomogeneously heated outer shell with a cold core. Bremsstrahlung emission of the free electrons scales as $n_e^2/\sqrt{T_e}$. A $n_e^2/\sqrt{T_e}$-weighted temperature distribution of the simulated droplet reveals that two temperatures at about 25

and 40 eV dominate for the simulated delay times, up to +70 fs after the laser pulse maximum.

In the experiment, a cryogenic hydrogen filament with a diameter of 8–10μm was irradiated by 800 nm laser pulses with a pulse duration of (80 ± 20)fs at an intensity of $2 \cdot 10^{16}$ W cm^{-2}. The resulting bremsstrahlung was measured by a focusing XUV spectrometer and corrected for all instrument characteristics. In the spectral range of 8–18 nm, the quality of the data allows fitting with a model based on Kramer's law, including the Gaunt factor in Sommerfeld approximation to account for medium and quantum effects. The best fit was obtained using two temperatures at ~13 and ~30 eV. The indication for two temperatures and their magnitude are in agreement with the PIC simulations. However, the lower temperatures in the experiment can be explained by missing energy-loss channels in the simulations, as well as the inclusion of hot, non-Maxwellian electrons in the temperature calculation.

We prove that bremsstrahlung spectroscopy can yield the temperature and density of free electrons on sub-picosecond time scales of the plasma evolution. Hence we resolved the time-scale for laser-heating of hydrogen, and PIC results for laser–matter interaction were successfully tested against the experiment data.

The presented method uses time-integrated continuum self-emission of a plasma in a spectral range similar to the dominant temperatures of free-electrons. As we have shown, it is only sensitive to areas with high free-electron density, and therefore limited to timescales shorter than hydrodynamic expansion. It may serve as a complementary diagnostic to pump-probe schemes such as collective x-ray scattering (plasmon spectroscopy) or x-ray absorption near-edge spectroscopy (XANES).

Acknowledgments

The assistance of the VolkswagenStiftung via a Peter-Paul-Ewald Fellowship, and the Alexander von Humboldt Foundation, the German Bundesministerium für Bildung und Forschung within the priority research area FSP 301/302, the Deutsche Forschungsgemeinschaft within the SFB 652, and CUI is acknowledged. Partial funding from UK EPSRC grant EP/G007187/1 and from the French Agence Nationale de la Recherche under Grant IRONFEL—ANR-12-PDOC-0011 is acknowledged. This work was partially performed under the auspices of the US. Department of Energy by Lawrence Livermore National Laboratory under Contract No. DE-AC52-07NA27344 and was supported by LDRD 11-ERD-050. It was also supported by the DOE Office of Science, Fusion Energy Sciences under FWP 100182. Simulations were performed at the John von Neumann-Institut for computing.

References

[1] Remington B A *et al* 2005 Accessing high pressure states relevant to core conditions in the giant planets *Astrophys. Space Sci.* **298** 235–40
[2] Drake R P 2009 Perspectives on high-energy-density physics *Phys. Plasmas* **16** 055501
[3] McMahon J M, Morales M A, Pierleoni C and Ceperley D M 2012 The properties of hydrogen and helium under extreme conditions *Rev. Mod. Phys.* **84** 1607
[4] Baraffe I, Chabrier G and Barman T 2010 The physical properties of extra-solar planets *Rep. Prog. Phys.* **73** 016901
[5] Hemley R J 2010 Percy W Bridgman's second century *High Press. Res.* **30** 581–619
[6] Guillot T 1999 Interiors of giant planets inside and outside the solar system *Science* **286** 72–77
[7] Nettelmann N *et al* 2008 *Ab initio* equation of state data for hydrogen, helium, and water and the internal structure of Jupiter *Astrophys. J.* **683** 1217–28
[8] Saumon D, Chabrier G and van Horn H M 1995 An equation of state for low-mass stars and giant planets *Astrophys. J. Suppl. Ser.* **99** 713
[9] Becker A *et al* 2014 *Ab initio* equations of state for hydrogen (H-REOS. 3) and helium (He-REOS. 3) and their implications for the interior of Brown Dwarfs *Astrophys. J. Suppl. Ser.* **215** 21
[10] More R M, Warren K H, Young D A and Zimmerman G B 1988 A new quotidian equation of state (qeos) for hot dense matter *Phys. Fluids (1958-1988)* **31** 3059–78
[11] Zastrau U *et al* 2014 Resolving ultrafast heating of dense cryogenic hydrogen *Phys. Rev. Lett.* **112** 105002
[12] Höll A *et al* 2007 Thomson scattering from near-solid density plasmas using soft x-ray free electron lasers *High Energy Density Phys.* **3** 120–30
[13] Zastrau U *et al* 2014 Equilibration dynamics and conductivity of warm dense hydrogen *Phys. Rev.* E **90** 013104
[14] Toleikis S *et al* 2010 Soft x-ray scattering using fel radiation for probing near-solid density plasmas at few electron volt temperatures *High Energy Density Phys.* **6** 15–20
[15] Leconte J and Chabrier G 2012 A new vision of giant planet interiors: impact of double diffusive convection *A&A* **540** A20
[16] Mackinnon A J *et al* 2012 Assembly of high-areal-density deuterium-tritium fuel from indirectly driven cryogenic implosions *Phys. Rev. Lett.* **108** 215005–9
[17] Glenzer S H *et al* 2012 Cryogenic thermonuclear fuel implosions on the national ignition facility *Phys. Plasmas* **19** 056318–32
[18] Regan S P *et al* 2012 Hot-spot mix in ignition-scale implosions on the NIF *Phys. Plasmas* **19** 056307–13
[19] Glenzer S H and Redmer R 2009 X-ray Thomson scattering in high energy density plasmas *Rev. Mod. Phys.* **81** 1625–63
[20] Fäustlin R R *et al* 2010 Observation of ultrafast nonequilibrium collective dynamics in warm dense hydrogen *Phys. Rev. Lett.* **104** 125002
[21] Gibbon P 2004 *Short Pulse Laser Interactions With Matter* (Singapore: World Scientific)
[22] Mulser P and Bauer D 2010 *High Power Laser-Matter Interaction, Springer Tracts in Modern Physics* vol 238 (Berlin: Springer Science & Business Media)
[23] Sperling P, Zastrau U, Toleikis S, Glenzer S H and Redmer R 2015 X-ray thomson scattering diagnostics of impact ionization in laser-driven carbon foils *J. Phys. B: At. Mol. Opt. Phys.* **48** 125701
[24] Bornath T, Hilse P and Schlanges M 2007 Ionization dynamics in nanometer-sized clusters interacting with intense laser fields *Laser Phys.* **17** 591–603

[25] Fennel T, Ramunno L and Brabec T 2007 Highly charged ions from laser–cluster interactions: Local-field-enhanced impact ionization and frustrated electron–ion recombination *Phys. Rev. Lett.* **99** 233401
[26] Toleikis S *et al* 2010 Probing near-solid density plasmas using soft x-ray scattering *J. Phys. B: At. Mol. Opt. Phys.* **43** 194017
[27] Rayleigh L 1879 On the capillary phenomena of jets *Proc. R. Soc. London* 29 71–97
[28] Ackermann W *et al* 2007 Operation of a free-electron laser from the extreme ultraviolet to the water window *Nat. Photonics* **1** 336–42
[29] Tiedtke K *et al* 2009 The soft x-ray free-electron laser FLASH at DESY: beamlines, diagnostics and end-stations *New J. Phys.* **11** 023029
[30] Redlin H *et al* 2011 The flash pump-probe laser system: setup, characterization and optical beamlines *Nucl. Instrum. Methods Phys. Res.* A **635** 88–93
[31] Fäustlin R R, Zastrau U, Toleikis S, Uschmann I, Förster E and Tschentscher T 2010 A compact soft x-ray spectrograph combining high efficiency and resolution *J. Instrum.* **5** P02004
[32] Zastrau U *et al* 2011 *In situ* determination of dispersion and resolving power in simultaneous multiple-angle XUV spectroscopy *J. Instrum.* **6** P10001–10
[33] Popov V S 2004 Tunnel and multiphoton ionization of atoms and ions in a strong laser field (Keldysh theory) *Phys.—Usp.* **47** 855
[34] Max C E, Arons J and Langdon A B 1974 Self-modulation and self-focusing of electromagnetic waves in plasmas *Phys. Rev. Lett.* **33** 209
[35] Brunel F 1987 Not-so-resonant, resonant absorption *Phys. Rev. Lett.* **59** 52–55
[36] Tajima T and Dawson J M 1979 Laser electron accelerator *Phys. Rev. Lett.* **43** 267
[37] Kruer W L and Estabrook K 1985 J × B heating by very intense laser light *Phys. Fluids (1958-1988)* **28** 430–2
[38] Pukhov A 2003 Strong field interaction of laser radiation *Rep. Prog. Phys.* **66** 47
[39] Liseykina T V, Pirner S and Bauer D 2010 Relativistic attosecond electron bunches from laser-illuminated droplets *Phys. Rev. Lett.* **104** 095002
[40] Zastrau U *et al* 2008 Bremsstrahlung and line spectroscopy of warm dense aluminum heated by XUV free electron laser *Phys. Rev.* E **78** 066406
[41] Zastrau U *et al* 2012 XUV spectroscopic characterization of warm dense aluminum plasmas generated by the free-electron-laser FLASH *Laser Part. Beams* **30** 45–56
[42] Griem H R 1997 *Principles of Plasma Spectroscopy* (Cambridge: Cambridge University Press)
[43] Kramers H A 1923 On the theory of x-ray absorption and the continuous x-ray spectrum *Phil. Mag.* **46** 836
[44] Gaunt J A 1930 Continuous absorption *Proc. R. Soc.* A **126** 654
[45] Fortmann C *et al* 2006 Bremsstrahlung versus Thomson scattering in VUV-FEL plasma experiments. *High Energy Density Phys.* **2** 57